Hot-electron energy coupling in ultraintense laser-matter interaction

A. J. Kemp,[1] Y. Sentoku,[2] and M. Tabak[1]
[1]*Lawrence Livermore National Laboratory, Livermore, California 94551, USA*
[2]*University of Nevada, Reno, Nevada 89577, USA*
(Received 12 March 2009; published 22 June 2009)

We investigate the hydrodynamic response of plasma gradients during the interaction with ultraintense energetic laser pulses using kinetic particle simulations. Energetic laser pulses are capable of compressing preformed plasma gradients over short times, while accelerating low-density plasma backward. As light is absorbed on a steepened interface, hot-electron temperature and coupling efficiency drop below the ponderomotive scaling and we are left with an absorption mechanism that strongly relies on the electrostatic potential caused by low-density preformed plasma. We describe this process, discuss properties of the resulting electron spectra and identify the parameter regime where strong compression occurs. Finally, we discuss implications for fast ignition and other applications.

DOI: 10.1103/PhysRevE.79.066406 PACS number(s): 52.57.Kk, 52.65.Pp

I. INTRODUCTION

While intense short laser pulses offer many interesting applications for high energy-density physics [1], coupling, and transport of energy into dense plasma in the ultrarelativistic intensity regime are poorly understood due to the complex dynamics near the absorption point, and difficult to model due to the several orders of magnitude between the dense-plasma response time and corresponding length and the scales of the laser spot size and pulse duration. An additional problem is the large scale, low-density blow-off plasma in front of the actual solid target found in high-energy short-pulse experiments. It is created before the arrival of the main pulse by amplified spontaneous emission processes in the laser that cannot be easily suppressed and is dense enough as to prevent light propagation several micrometers away from the target.

As the formation of the preformed plasma occurs on a nanosecond time scale, it cannot be self-consistently included in the kinetic models that are currently used for short-pulse interaction because those are limited to picosecond time scales for technical reasons. Instead, the preformed plasma is usually modeled in separate hydrodynamic simulations.

For a recent high-energy short-pulse experiment, scale lengths of about 0.5–1.0 μm between solid density and a fraction of the critical density $n_c=1.1\times10^{21}$ cm^{-3} were found preceded by longer scale length plasma [2]. In future fast ignition experiments, one expects scale lengths of up to 10 μm depending on the energy in the prepulse.

This paper addresses the short-pulse laser-driven dynamics of preformed plasma in the limit of ultraintense, energetic pulses over a picosecond. At intensities $I_L=1.37\times10^{20}$ W/cm^2 the vacuum-energy density of light corresponds to $\geq$30 Gbar at 1 μm wavelength light. Such a pressure can cause ions to move over several microns in less than 1 ps [3]. Many early works on absorption consider idealized step-function density profiles, relatively short density gradients, or large volumes [4,5], effectively neglecting the large-scale ion motion. We characterize the response of plasma gradients in the limit of normal incidence with one spatial and three velocity (1D3V) degrees of freedom in a fully relativistic kinetic description. Our approach allows us to isolate 1D "hydrodynamic"–from purely multidimensional effects such as beam filamentation [6], hole boring [7], and deformations of the plasma surface through Rayleigh-Taylor like instabilities [8]. We ignore refluxing of hot-electrons, which can occur due to electrostatic confinement in thin foils.

First we consider two plasma density gradients with different scale lengths. Both cases show how the laser-generated ponderomotive pressure near the relativistic critical density causes a strong compression of the preplasma toward higher densities and acceleration into vacuum of plasma at lower densities, followed by a drop in absorption and hot-electron temperature. To understand this, we study simple step-function density profiles where the ion motion is suppressed. Here we find key properties of the laser-generated electron distribution at ultrarelativistic intensities; expressions for cut-off energies and temperatures are given. Combined with an analytical description of the compression, which depends on plasma scale length, ion charge-to-mass ratio and laser intensity, wavelength and pulse duration, this is useful for defining plasma parameters at which absorption remains high over the laser pulse duration and electron temperature is within the parameter band for fast ignition or other applications [1].

Finally we study the generation of the "hot" tail of the electron distribution functions found in all our simulations. We demonstrate that the hot tail originates in the underdense plasma in front of the dense-plasma interface. We then discuss the relationship between the *in situ* distribution of electrons in the underdense plasma and the hot tail we find inside the solid density plasma; and discuss qualitatively how electrons are accelerated to energies far beyond the laser ponderomotive potential in quasiexponential distributions.

Simulations were performed with a 1D3V particle-in-cell code (PIC) [9] using a resolution of 500–1000 cells per laser wavelength and up to 300 particles per species and cell, thus resolving the plasma's Debye length at the highest density and initial temperature of 10 keV and verified with an up to 3$\times$ higher resolution. Resistive processes are not included in our study, which is merely aimed at characterizing the laser-

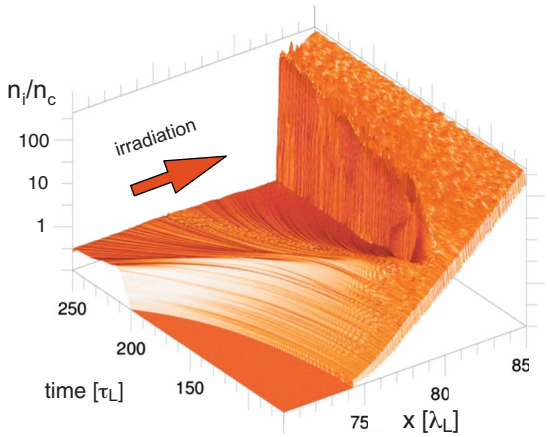

FIG. 1. (Color online) Deformation of an exponential density gradient with scale length $l_s=0.85$ μm and peak density $n_{i,\max}=400n_c$, irradiated by a laser pulse with intensity $I_L=1.37\times10^{20}$ W/cm^2, wavelength/period $\lambda_L=1$ μm, $\tau_L=3.3$ fs.

electron coupling and not transport in dense plasma. The latter will be subject of a separate study.

II. INTERACTION WITH A DENSITY GRADIENT

Figure 1 depicts the evolution of an initially exponential plasma profile during the interaction with an ultraintense laser pulse. Shown is a contour plot of ion density versus space and time for a gradient scale length of 0.85 μm, beginning at time $70\tau_L$, where $\tau_L\equiv\lambda_L/c\approx3.3$ fs is the laser period and $n_c=\pi m_e c^2/(e\lambda_L)^2$ is the critical density. Between 90–100 μm the density profile is uniform, representing a solid target region. Plasma ions have a mass $M_i=8m_p$ where m_p is the proton mass and charge state $Z=1$. Light enters the box at $x=0$ with an intensity of 1.37×10^{20} W/cm^2 at $\lambda_L=1$ μm, and a semi-infinite pulse envelope. The vacuum region between the left box boundary and the plasma gradient allows for a free expansion over the simulation time of $350\tau_L$. Electrons leaving the box at the right are reinjected with a thermal random distribution, so that they will not "reflux" with their original energy once they have entered the solid density region of the target.

Figure 2 gives details of this "short gradient" (SG) case shown in Fig. 1 and a "long gradient" (LG) case with a scale length of 3.25 μm. Shown are snapshots of ion density as well as corresponding electron spectra and electron energy flux density recorded in the solid density region

$$W_{e,x}=\int_{x=x_d} dv(df/dv)(\gamma-1)v_x, \tag{1}$$

averaged over a laser cycle and normalized to the average laser energy flux $\langle W_L\rangle=I_L/2$. We have checked that energy flux and spectra are independent of where exactly in the solid target region they are recorded. Additionally, spectra of all electrons passing through a single cell over a $10\tau_L$ time interval give nearly identical results. Figures 2(a) and 2(b) show electron spectra for the LG and SG cases at two times, illustrating how they evolve from initially similar characteristics in temperature and number to quite different regimes at a later time when hydrodynamics has changed the shape of the gradient. The LG spectrum maintains its high-energy tail at ~6 MeV consistent with the ponderomotive scaling [10], while in the late SG spectrum high-energy particles have almost disappeared. Also, the average energy of the low-energy hot-electron population (slope temperature <1 MeV at 250 fs) in SG is smaller than in LG by the square root of the density ratio at the steepened interface, compare Fig. 2(e) [11]. Figure 2(c) gives the time dependence of the electron-energy flux $\langle W_{ex}\rangle/\langle W_L\rangle$ in both cases. Figure 2(d) shows corresponding ion density profiles at two times. In both cases, coupling of the intense laser pulse drives an electrostatic shock wave toward the solid at a speed of $\approx0.01c$ [12–14],

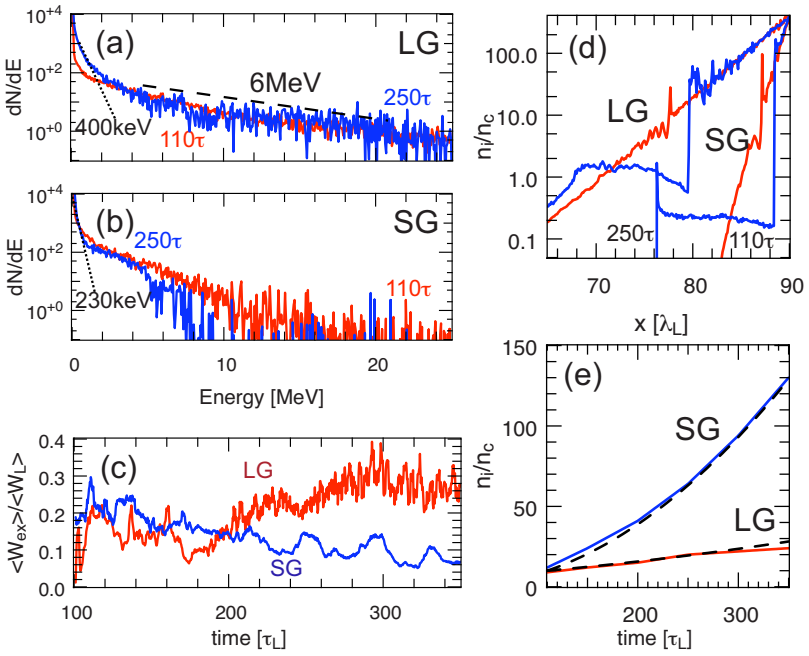

FIG. 2. (Color online) Absorption and electron transport in exponential density gradients at $I_L=1.37\times10^{20}$ W/cm^2. (a) Electron spectra at two times for a LG case with $l_s=3.25$ μm; (b) for a SG with $l_s=0.85$ μm; (c) average electro-energy flux density $\langle W_{ex}\rangle$, normalized to the laser intensity W_L for SG and LG, recorded behind the density gradient at $x_d=95$ μm; (d) snapshots of ion density at $t=110,250\tau_L$; (e) front density vs analytical result (dashed).

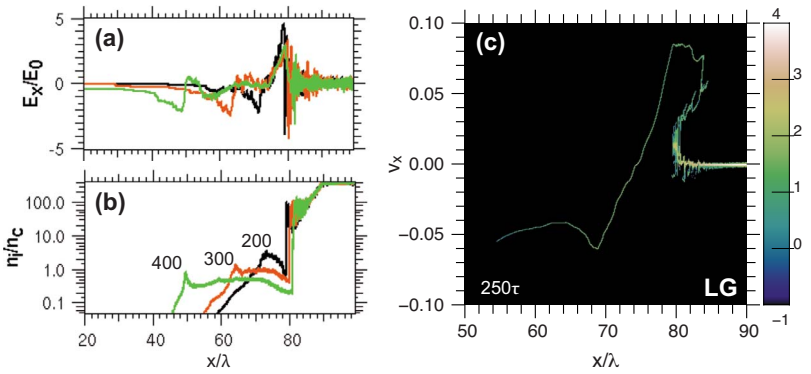

FIG. 3. (Color online) Long-term evolution of the plasma near interaction point; (a) electric field E_x at times 200, 300, and $400\tau_L$; (b) ion density at the same times; (c) Ion phase space in the LG case at time $250\tau_L$.

while it accelerates plasma backward forming a flat "lower shelf." Two remarkable differences between these two cases are (a) a 4× higher density of the lower shelf plasma at $250\tau_L$ in the LG case and (b) its 4× lower density of the "upper shelf" plasma, while the electron-energy spectrum has a shoulderlike shape. These lead to differences in absorption discussed below. Additional simulations at a hundred times reduced laser intensity show a much lesser impact on the plasma profile leading to a nearly constant absorption of roughly 30%.

The compression of the plasma gradient shown in Fig. 2(e) can be described using momentum conservation at the front, i.e., where light is reflected [7,8]

$$(1+R)I_L/c = 2M_i u_f^2 n_i \tag{2}$$

in a frame moving at velocity u_f with the front. Here $R \approx 1$ is a good approximation of the 1D plasma reflectivity and n_i is the ion density, neglecting electron momentum. This is valid only in the ultrarelativistic case [7]. Reflection occurs at an electron density $\gamma_{os} n_c$ with $\gamma_{os} = \sqrt{1+\langle a^2 \rangle}$ [5,8], where a is the effective normalized amplitude including the reflected light related to the intensity via $I_L/c = m_e c^2 n_c a_0^2/2$ for a laser wavelength of $\lambda_L = 1$ μm. Below this density, electrons are accelerated to relativistic Maxwellian distributions with average energy $m_e c^2(\gamma_{os}-1)$, consistent with Figs. 2(a) and 2(b). The time-dependent compression of a profile $n_i(x) = (\gamma_{os} n_c/Z)\exp[(x-x_c)/l_s]$ with scale length l_s is obtained by solving Eq. (2) for u_f and integrating

$$x_f(t) = x_c + 2l_s \ln\left[1 + t\frac{c}{2l_s}\left(\frac{m_e Z}{2M_i}\frac{\gamma_{os}^2 - 1}{\gamma_{os}}\right)^{1/2}\right] \tag{3}$$

to find the location of the front [3]. Figure 2(e) plots the corresponding interface density at the front vs time and simulation results. Expansion of the plasma toward vacuum is characterized by that fact that the outwardly accelerated mass is nearly constant and by $v_i \propto (x-x_c)\times(t-t_0)$, forming a density plateau. The ion bump at the front of the expansion has been discussed earlier [15].

Figure 3 shows the structure of the ion phase space at $250\tau_L$, as well as that of the longitudinal electric field and the ion density at late times for the case of the LG. In one spatial dimension the plasma expansion leads to a monotonic drop of the ion density near the critical interface and eventually a drop of the electric field. While we expect this to cause a drop in the 1D absorption over a picosecond time scale for reasons explained below, it is worth pointing out here that the compression is likely over emphasized in 1D simulations; when transverse degrees of freedom are available to the plasma near the point of interaction, the surface dynamics is more complex [8].

III. ELECTRON ACCELERATION NEAR HIGH-DENSITY INTERFACE

In order to understand the evolution of absorption and electron flux in the density gradients above, we now turn to a "quasistatic" scenario in which the ion motion is suppressed. Instead of an exponential ramp, we use a 3 μm layer of lower shelf plasma at uniform ion density n_s in front of a 10 μm layer of plasma at 'solid' density $200n_c$ (in most cases). Figure 4 shows electron spectra, electrostatic field near the boundary for several densities n_s, as well as cycle-averaged electron-energy flux $\langle W_{ex} \rangle / \langle W_L \rangle$. Locations of

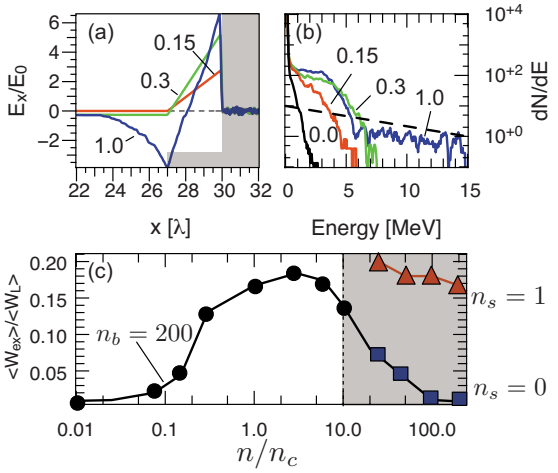

FIG. 4. (Color online) Absorption and electron transport in step-function density profiles at $I_L = 1.37\times10^{20}$ W/cm^2. (a) Electron spectra for various values of the shelf density parameter n_s/n_c as indicated. Dashed line gives a 6.7 MeV slope temperature; (b) corresponding snapshots of E_x; location of shelf and bulk target are indicated by shaded area; (c) laser-to-electron coupling efficiency vs. plasma density. For $n_s \leq 10$, targets consist of a 3 μm long lower shelf at density n_s followed by 10 μm of plasma at $200n_c$; for $n_s \geq 10$ plasma is uniform. Rectangular symbols refer to $n_s = 0$, triangles to $n_s = 1$.

lower shelf and bulk plasma are indicated by a shaded area in Fig. 4(b).

Depending on the density-length product of the lower shelf, electrons are pushed into the bulk by the ponderomotive pressure. The maximum arial charge that can be pushed into the bulk is determined by a balance between the laser and electrostatic field energy

$$2I_L/c = en_s\phi_s, \tag{4}$$

with $\phi_s = 2\pi e n_s l_s^2$, assuming no absorption. Normalization yields $a_L^2 = 2\pi^2 (n_s/n_c)^2 (l_s/\lambda_L)^2$. For $a_L = 10$ and $l_s = 3$ μm, we find $n_{s,0} = 0.75 n_c$ for the "critical," i.e., maximum density that can be pushed into the bulk. On the other hand, by fixing $n_s = n_c$ we get a maximum shelf length of 2.25 μm consistent with Fig. 4(b), where $E_0 = m_e \omega c/e$. The maximum electric field at the interface $E_{x,\mathrm{i}}^{\max} = a_0/\sqrt{2}$ is reached when the shelf arial density $n_s l_s$ of Eq. (4) is critical, which also agrees with Fig. 4(b) after accounting for some absorption; see Fig. 4(c). As the electric field at the interface increases with n_s, the electron spectrum extends to higher maximum energies and forms a shoulderlike distribution. When the lower shelf density exceeds the critical value, here $n_s \geq n_c$, hot-electrons that remain in the shelf cause an ambipolar electrostatic field and an additional tail in the distribution function appears [8] that is absent for smaller values of n_s.

Key features of the spectra are reproduced by a simple model of electron acceleration near a shelf-solid density interface described in the following. The electric and magnetic fields E_y, B_z of a linearly polarized light wave in front of an almost perfectly reflective, semi-infinite plasma at $x > 0$ are given by a standing-wave structure [16]

$$E_y = 2a_0 \sin(2\pi x + \phi)\cos(2\pi t)$$

$$B_z = 2a_0 \cos(2\pi x + \phi)\sin(2\pi t), \tag{5}$$

where $\tan(\phi) = -\sqrt{n_c/n_p}$ and E and B are given in normalized units $E_0 = m_e \omega_0 c/e$ and $B_0 = m_e \omega_0/e$. Let us now assume that at time $t = 0$ a test-particle electron is extracted from the plasma by an electrostatic field E_x oriented normal to the interface. As mentioned before this electrostatic field is due to a noncharge-neutral shelf region at $x < 0$. As soon as the particle enters the shelf region, the laser electric field accelerates the electron in the transverse direction. Note that the initial temperature of the plasma determines at what rate electrons are extracted, see the comment at the end of this section. Due to the constant phase relation between the laser electric and magnetic field, the magnetic contribution to the Lorentz force $B_z v_y$, where $B_z \approx 2a_0 \sin(2\pi t)$ near the interface, converts transverse into longitudinal momentum directed back into the target, as soon as $|B_z v_y| > |E_x|$.

The time at which the electron turns around can now be estimated by integrating the equation of motion

$$\partial p_x/\partial t = -2\pi E_{x,\mathrm{i}} + 4\pi a_0 \sin(2\pi t), \tag{6}$$

assuming that $v_y \approx -c$ and using normalized momenta $p \equiv p'/m_e c$, as well as velocities $v/c = p/\sqrt{1+|p|^2}$ and time $t \equiv t'/\tau_L$. Solving numerically for $p_x(\Delta t) = 0$ in the case of a critical-density plasma shelf, we find $\Delta t \approx 0.12\tau_L$. At this time the test particle is located at $x \approx -c\Delta t$ and is accelerated back into the plasma. The time that passes before the test electron reaches the plasma again and is not accelerated further, is similar to Δt. During this time it can gain a longitudinal momentum

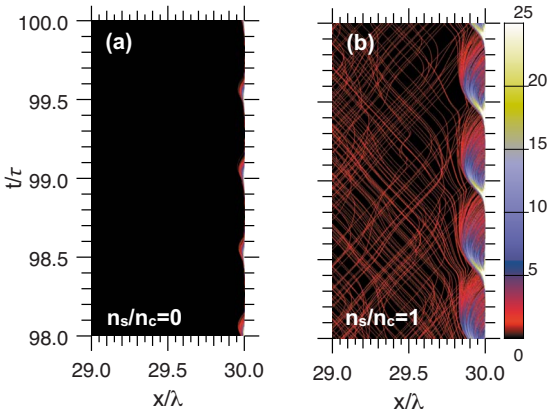

FIG. 5. (Color online) Spatio-temporal evolution of the electron density n_e/n_c near density step, with and without preplasma. Solid density plasma begins at $x = 30$ μm. underdense plasma in (b) extends to 27 μm.

$$p_x^{\max} \leq 4\pi a_0 \Delta t \approx 1.45 a_0. \tag{7}$$

For $a_0 = 10$ this expression predicts a cut-off energy $E_{\max} \approx 7$ MeV, in agreement with Fig. 4(a), curve labeled "0.3." The shoulderlike feature of the spectrum stems from (i) electrostatic shielding of electrons extracted during the time interval $[0, t']$ by the charges of other electrons and (ii) their relative phase with respect to the electromagnetic field pattern. For larger amounts of lower shelf plasma, the "shoulder" remains unchanged and an additional tail of hot-electrons appears that originates in the low-density plasma where both light and plasma are present [8]. For an undercritical lower shelf, where E_x is determined by the arial charge $n_s l_s$, the spectrum is independent of intensity, because $t' \propto E_{x,\mathrm{i}}/a_0$ while $p_x^{\max} \propto a_0 t'$. We have verified this by simulations at different laser amplitudes not shown here. Without the lower shelf plasma there is no electrostatic extraction of electrons, so acceleration occurs in the evanescent mode of E_y, giving a much smaller absorption scaling with density as $1/\sqrt{n}$ [11]. The extraction/acceleration process repeats itself at time $\tau_L/2$ with $p_y > 0$, leading to the well-known $2\omega_0$ electron jets [4], compare Fig. 5. Figure 4(c) plots time-averaged electron flux (absorption) vs plasma density in a combination of two separate scenarios: at low-density $n/n_c < 10$, density refers to a 3 μm thick lower shelf preceding a 10 μm layer of bulk plasma at a constant density of $200 n_c$, compare Fig. 4(a). Light propagates through the lower shelf plasma because it is relativistically undercritical [5]. For higher densities $n/n_c \geq 10$, the plasma becomes opaque. Here, the quantity n refers to the density of a 10 μm thick uniform plasma layer; both scenarios give the same result for $10 n_c$.

The effect of changing the bulk plasma density while keeping $n_s/n_c = 0.1$ is small, as shown in a separate curve. Comparison of this curve for $n_s/n_c = 1$ (triangles) with the

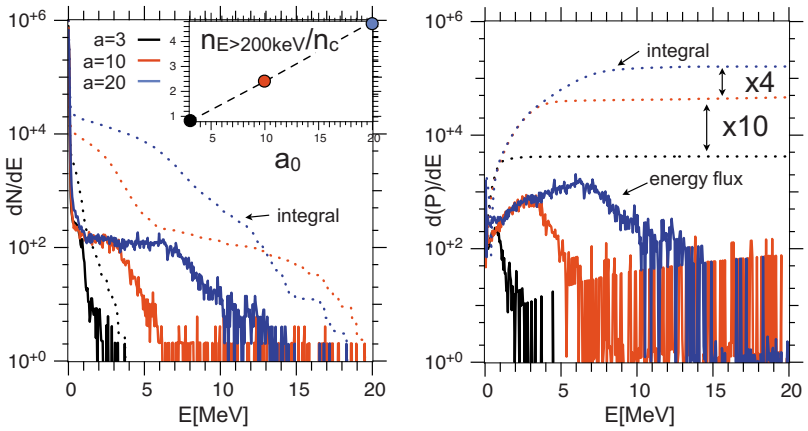

FIG. 6. (Color online) Intensity scaling of electron spectra and absorption in step-function density profiles; electron energy (a), and energy flux spectra (b) for three laser intensities. Plasma configuration identical to Fig. 4, using 3 μm of underdense plasma at $1n_c$ followed by $200n_c$ solid density. Inset shows hot-electron density vs a_0.

$n_s=0$ curve (rectangles) demonstrates that (1) absorption depends critically on the preplasma; (2) it is nearly independent of bulk density with $n_s/n_c \geq 1$; and (3) it drops slightly with bulk density when $n_s \ll n_c$. This is representative of the decrease in absorption seen in Fig. 2, where the lower shelf density drops due to the hot-electron pressure, while the interface is compressed, over time. In one spatial dimension, the only way to slow this effect down is by choosing larger gradient lengths for the preformed plasma, i.e., more energy in the prepulse or lower intensities. We expect that this effect is diminished in 2D. For $n_b > 50n_c$ absorption is very small, i.e., $<5\%$ and almost independent of plasma density. When repeated for different intensities with $a \gg 1$, the laser-to-electron coupling efficiency curve shown in Fig. 4(c) mostly maintains its shape, its maximum is shifted to the relativistic critical density $n_{cr} \approx n_c \times (1+a_0^2)^{1/2}$ [11].

Figure 5 illustrates the acceleration of electrons in front of the dense-plasma interface by showing the spatio-temporal evolution of the electron density around the interface located at $x=30$ μm with and without preplasma. The laser electric field has the structure of a standing wave with the fundamental laser wavelength and an amplitude twice the vacuum amplitude. When preplasma is present, the field is only slightly distorted compared to the perfectly reflecting case.

Having discussed the role of the preformed plasma on absorption for one specific intensity, we will now fix the plasma profile and show how electron spectrum and absorption varies with laser intensity, within a parameter range relevant to fast ignition.

Figure 6 shows the dependence of the spectra of electron energy and energy-flux density on laser intensity, for a plasma setup with 3 μm of underdense plasma at $1n_c$ followed by $200n_c$ solid density plasma, i.e., three cases centered around the one discussed in Fig. 3. The laser intensity is varied between $a_0=3$, corresponding to 1.2×10^{19} W/cm^2, and $a_0=20$, corresponding to 5.5×10^{20} W/cm^2 at a 1 μm wavelength. In both plots we focus on an energy window in which most of the total energy and energy flux are contained. Also shown are integrals of electron density and energy flux density for each case. Both the direct particle energy spectrum and the hot-electron density scale with the normalized laser amplitude. As a result, the electron energy flux is a constant fraction of the laser intensity, or, in other words, the absorption fraction is independent of laser intensity.

Figure 6(a) also gives the integrated hot-electron density up to an energy E as the total number of particles with energies greater than E. All spectra are taken in a spatial window over 5000 cells inside the solid part of the target, using 100 particles per cell representing a density of $200n_c$. We can now directly read off the density of hot-electrons beyond a certain energy E. There is a linear scaling with laser amplitude, we find the maximum density of "hots" to vary between $0.5-5n_c$. The scaling of n_{hot} with laser amplitude a_0 is shown in the inset of Fig. 6(a), using a lower cutoff of 200 keV. Figure 6(b) shows the integrated hot-electron energy flux, allowing us to calculate the conversion ratio by comparing the electron energy flux to the average laser flux $a^2/2$. In all three cases we find that roughly 18% of the laser energy is converted into hot-electrons consistent with Fig. 4. The integral curves further show that the maximum energy flux lies at roughly the ponderomotive potential a_0 of the laser pulse and scales linearly with a_0.

In order to compare our results to a standard case from the literature, we have performed a simulation of a step-function density profile with mobile ions at a density $100n_c$ and an intensity $I_L=10^{18}$ W/cm^2, finding an absorption fraction of 14% for an initial electron temperature of 10 keV, which is in good agreement with results published earlier [4]. This is relatively high, compared to the $<1\%$ value we find for cases without preplasma in Fig. 4(c) above. It is caused by thermal expansion of the bulk plasma and the subsequent formation of a density gradient similar to the ones discussed above. In runs at the same intensity but with initially cold electrons, i.e., <1 keV, or at higher intensities around 10^{20} W/m^2, the expansion is suppressed by the ponderomotive pressure and absorption drops back to $<1\%$. This means that it is important to include the right amount of preformed plasma in simulations at high laser intensities [17]. We find that the initial electron temperature is much less relevant in our density gradient simulations.

While collisions play no direct role for absorption in plasma density gradients around $10-30n_c$ and keV temperatures, they could contribute indirectly by causing electrostatic fields in resistive, dense plasma. Resistive electric fields could cause slowing down and refluxing of hot-electrons even in large fast-ignition relevant targets, enhance absorption and electron temperature and possibly change the nature of the return current via runaway processes [18]. This is currently under investigation.

Results are scalable with respect to laser wavelength using the relation $I\lambda_L^2 \propto a_0^2$, i.e., for a given intensity a smaller wavelength leads to smaller a_0. Under oblique incidence, absorption tends to be higher than under normal incidence because the laser electric field has an angle $\alpha < 90°$ to the target surface [19,20]. For small α, this will affect the momentum balance Eq. (2) in that the Poynting flux is reduced by a factor cos α, so that we do not expect drastic changes.

Backscattering of the ultraintense light in underdense plasma is found to be only a minor effect, in terms of the power balance; however, it is crucial for key aspects of the observed spectra as will be explained below. Current filamentation in low-density plasma will alter absorption for large-scale lengths $l_s > 1$ μm, but for the short gradient case presented in Fig. 1 we expect hydrodynamic effects to dominate depending on laser spot size etc.

The effective temperature T_{eff} for the hot tail accelerated in underdense plasma in front of a plasma mirror can be found using $a = 2a_0$ for the total (as opposed to incoming) field amplitude, compare Eq. (5) and the expression $T_{\text{eff}} = m_e c^2(\gamma_{\text{os}} - 1)$ with $\gamma_{\text{os}} = \sqrt{1 + \langle a^2 \rangle}$ [8]. For $a_0 = 10$ we have $\gamma_{\text{os}} \approx 14$ giving $T_{\text{eff}} \approx 6.7$ MeV in good agreement with our simulation results, compare Fig. 4(b). This temperature is much larger than the one found analytically in Ref. [21], which gives $T'_{\text{eff}} = 1.5$ MeV for a laser amplitude $a_0 = 10$. The main difference is that in our idealized simulations light is either reflected off a steep interface, or it interacts with underdense plasma, while Ref. [21] assumes that there is a density gradient that is on the same order as the laser wavelength. While we agree with the conclusion of Ref. [21] that the density gradient strongly affects the generated electron spectrum, our simulations indicate that this gradient becomes steeper over time, compare our Fig. 3. This figure shows the structure of the plasma electron density up to ≈ 1.2 ps, indicating a long underdense preplasma and a steep interface. While the latter leads to electron spectra dominated by the mechanism described above, the laser interaction with the former is responsible for the hot tail of the electron spectrum.

IV. ELECTRON ACCELERATION IN UNDERDENSE PLASMA

The so-called hot tail of the electron spectra mentioned above extends up to energies corresponding to several times the laser ponderomotive potential, compare Fig. 6. That makes it a highly visible feature of the spectrum since only energetic electrons can escape the electrostatic potential around laser-irradiated targets. The hot tail is generated during all stages of the interaction in the underdense blow-off plasma that forms already during the prepulse interaction as will be demonstrated below, but it carries only an insignificant fraction of the total energy flux compare Fig. 6(b). While measuring the energy spectrum of escaping electrons is an important experimental diagnostic, only computer simulations allow a direct comparison between the *in situ* spectra, as discussed here, and those of *escaping* electrons. This comparison is the subject of a separate study in preparation.

Quantitative features of the hot spectrum depend on the circumstances of their generation, i.e., laser pulse energy and duration, dimensions of the focal spot, plasma density, and profile. In this paper we focus on (a) the relationship between the spectrum found in the underdense plasma and spectra observed inside the solid target as discussed in the simulations shown above; and (b) the physical mechanism that is responsible for accelerating electrons in underdense plasma into a thermal spectrum with energies far beyond the ponderomotive potential. Note that we are not interested in the trapping of electrons in plasma waves that is relevant for plasma-based electron acceleration schemes [22]. While trapping can lead to electron energies more than one hundred times the ponderomotive potential, it leads to nonthermal, quasimonoenergetic spectra, and it affects only a small fraction of the plasma electrons and is irrelevant for fast ignition applications.

Figure 7 discusses the relationship between the electron spectrum generated in the underdense plasma and the hot tail of the spectrum found inside the solid target. Figure 7(a) shows the longitudinal electron phase space around the preplasma solid interface at time $90\tau_L$ for a case with 10 μm of preplasma at density $1n_c$ followed by a bulk plasma at $200n_c$ irradiated by a pulse with $a_0 = 10$ such as the ones discussed in Figs. 4 and 5. The maximum longitudinal momentum of electrons trapped in the potential well around the preplasma, as shown in Fig. 7(a) corresponds to a kinetic energy of around 40 MeV. This is about equal to the depth of the potential well shown in Fig. 7(b), which makes sure that electrons cannot escape to the left. The potential difference between the center of the preplasma where the electron momenta are maximum and the solid interface is about 25 MV. This value is roughly consistent with what we expect from the energy conservation argument in Eq. (4) compare Fig. 4. Here we can compute the electric potential difference between the center of the shelf plasma at $x = 28$ μm and the beginning of the solid density plasma at $x = 30$ μm by integrating the electric field for $n_s/n_c = 1$ giving roughly 22 MV.

Figure 7(c) compares a time-integrated electron spectrum obtained at the center of the potential well to one inside the solid density plasma; after shifting the shelf spectrum down by 25 MV, we obtain a spectrum that resembles the tail of the distribution found inside the target. This demonstrates that the hot tail of the distribution originates from the interaction of the laser pulse with the underdense preformed plasma. We have further verified this statement by labeling individual particles by their initial position as shown in Fig. 7(d); here we compare three electron spectra taken at time $40\tau_L$ in the solid part of the target. Shown are the spectrum of all electrons, electrons that originate in the solid part of the target, labeled as "w=2" as well as that of electrons originating from the shelf plasma region, labeled as "w=0.01." The isolated spikes in the tail of the spectrum, labeled by "(i)," correspond to particles that originated in the solid part of the plasma, then moved into the underdense shelf region as part of the return current and were later reaccelerated into the target; this history is confirmed by tracking the trajectories of several particles. This complex 1D history illustrates the difficulties of tracking individual particles in particle codes. It also explains why we have chosen an earlier time for Fig.

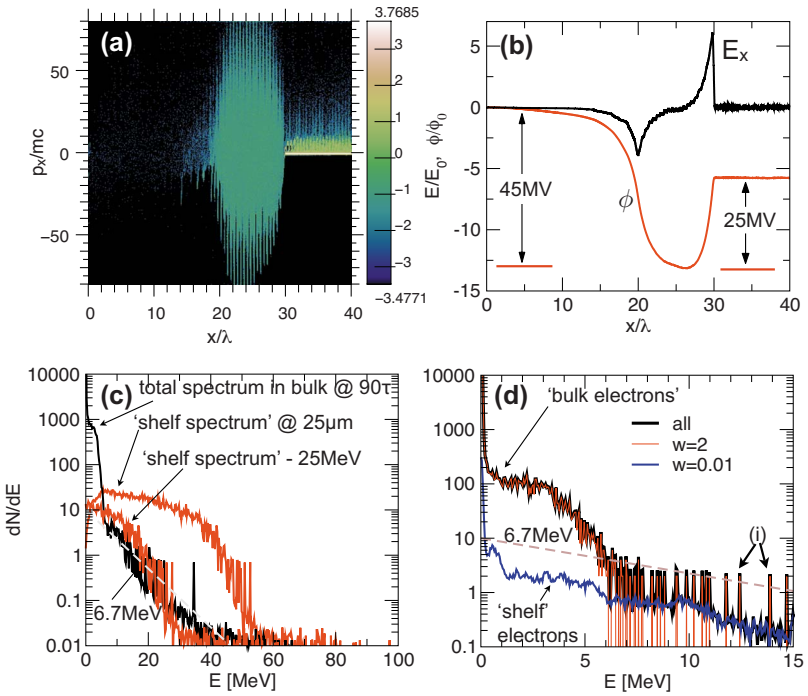

FIG. 7. (Color online) Electron acceleration from underdense plasma in step-function density profiles; (a) longitudinal electron phase space; (b) electric field and its potential; (c) comparison of electron spectrum in underdense plasma to that in solid and shifted underdense spectrum; (d) decomposition of electron spectrum in solid region by their origin; underdense labeled w=0.01, solid labeled w=2; label (i) refers to particles from underdense whose trajectories have been tracked, see text.

7(d), compared to the previous cases where all quantities are plotted at time $100\tau_L$. Note the difference in energy scale between Figs. 7(c) and 7(d). Also shown are lines corresponding to slope temperatures of 6.7 MeV in Fig. 7(c) and 7(d), as explained in Sec. III.

A. Hot-electron generation in underdense plasma

Electron acceleration in underdense plasma has been discussed in the context of many applications, e.g., laser wakefield acceleration, inertial confinement fusion, and fast ignition. Various mechanisms have been proposed such as plasma wave acceleration, direct laser acceleration, mixed acceleration from transverse and longitudinal fields [4,19], and chaotic motion in counterpropagating laser pulses [23–25]. The latter concept emphasizes the single-particle aspect of the interaction noting that electron motion transitions from regular to chaotic when a certain threshold amplitude for counterpropagating laser pulse is exceeded; this approach focuses on the interaction with transverse electromagnetic fields [23–25]. On the other hand, the role of the longitudinal electric field for the generation of quasithermal hot-electron distributions has been recognized by Ref. [26] in the context of resonance absorption. The central point of this section is to emphasize the importance of both fields.

In the following we discuss how electrons in the high-energy tail of the spectra shown above are accelerated beyond the laser ponderomotive potential and why the spectrum resembles a thermal spectrum despite its collisionless nature. Since this high-energy tail is a common feature of electron spectra observed in experiments with long scale-length plasma density gradients, we consider stretches of purely underdense plasma. The role of ion motion can be excluded; we observe no qualitative difference between electron spectra in simulations with or without ion motion.

We find that the essential ingredients for the generation of the high-energy tail is the combination of (1) counterpropagating laser pulses and (2) a background plasma that introduces a stochastic element to the electrons' equation of motion. With these two elements, the exponential character of the electron spectra can be explained as the result of a random-walk process where electrons are accelerated to multiples of the ponderomotive potential in the laser field while being scattered off a strong electrostatic wave. On the one hand, without strong plasma waves, electrons get accelerated to the ponderomotive potential of the laser pulse(s) and return their kinetic energy after the pulse has passed by [27]. On the other hand, without the presence of a counterpropagating laser pulse, i.e., when there is only one laser pulse present, electrons are not accelerated beyond the ponderomotive potential.

Figure 8 demonstrates the role of the longitudinal electric field for the generation of a hot thermal electron population. Shown are the results of 1D PIC simulations of the interaction of semi-infinite laser pulses with underdense plasma of different lengths and densities. In all simulations the ions are immobile, plasma is resolved with 60 cells per laser wavelength and we use 20 electrons per cell. All laser pulses have a rise time of 10 laser cycles, plasma is surrounded by 30 μm of vacuum on both sides. For one injected pulse and a plasma length of $L=50$ μm, we find a similar results as those discussed in Sheng *el al* [24], i.e., a spectrum with its peak near the ponderomotive potential of the laser pulse $a_0=3$. If the plasma length in a similar simulation is $L=500$ μm, however, we find a much greater fraction of high-energy electrons at a higher temperature. The reason of this difference is the relevance of the background plasma. While in the first case the box has a total size of only $5\lambda_p$, where $\lambda_p=\lambda_0/\sqrt{n_p/n_c}$ is the plasma wavelength, it is ten times larger in the second case. Figure 8(b) shows electron spectra for the case of two counterpropagating injected pulses. At the

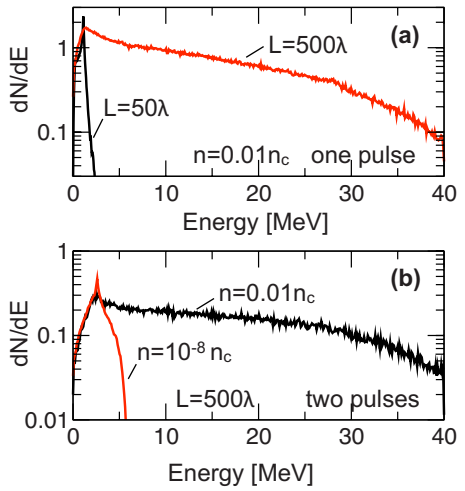

FIG. 8. (Color online) Role of longitudinal electric field for underdense plasma interaction. Electron spectra for different plasma length L, density n, and one/two pulse(s) at $I\lambda_L^2=10^{19}$ W/cm^2; (a) one pulse, vary plasma length; (b) two pulses, vary plasma density.

same plasma density $n_p/n_c=0.01$ as used above we get a roughly similar result. With vanishing plasma density $n_p/n_c=10^{-8}$, however, the spectrum is not thermal, and the maximum energy is ≤ 2 MeV. Here electrons behave more like single particles in a laser pulse [27].

Even though we present an electron spectrum generated by a "single injected pulse" traveling through underdense plasma in Fig. 8(a), there is usually an intrinsic Raman or Brillouin back-scattered pulse going in the opposite direction. In the case above, for example, we find about 10% reflectivity. In order to illustrate the importance of the counterpropagating wave for a thermal electron distribution, we have performed "reduced" 1D particle simulations where back scattering in the plasma has been suppressed. These test runs differ from regular PIC simulations in that transverse currents are artificially set to zero. This removes the reflected light wave, while still allowing for particle acceleration as well as plasma waves.

Figure 9 discusses the result of a test simulation of counterpropagating laser pulses through plasma with no transverse currents at laser amplitudes $a_0=1$ for both pulses. Figure 9(a) shows the longitudinal electron phase space at time $300\tau_L$. One can see that where both pulses overlap, electrons gain momenta higher than the combined pulses' ponderomotive potential and the distribution becomes quasithermal, as shown in Fig. 9(b). In regions where only one pulse is present, particle spectra resemble the case with "vanishing" plasma density discussed above.

The striking difference between spectra with only one injected pulse and those where both pulses are present, under otherwise identical conditions, demonstrates the importance of the counterpropagating pulse, see Fig. 9(b). On the other hand, the resemblance between the energetic spectra in Figs. 8(a) and 8(b) for one and two pulses in plasma including the physics of backscatter demonstrates how insensitive the acceleration is to the relative amplitude of the reflected light.

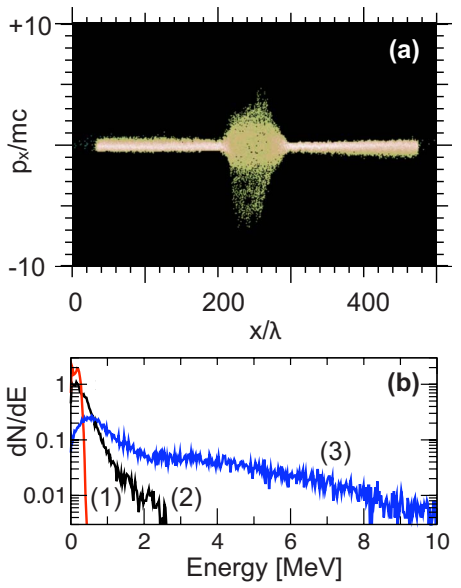

FIG. 9. (Color online) Electron acceleration by two counterpropagating pulses at $a_0=1$ in underdense plasma with reduced simulation; (a) longitudinal electron phase space at time $300\tau_L$; (b) electron spectra for $100<x/\lambda_L<200$ at time $300\tau_L$, labeled (1), for $200<x/\lambda_L<300$ at time $300\tau_L$, labeled (2), and for $100<x/\lambda_L<200$ at time $1000\tau_L$, labeled (3).

V. CONCLUSION

Preformed plasma is essential for high absorption at MeV electron energies in ultrahigh intensity short-pulse laser experiments. At intensities around 10^{20} W/cm^2 the ponderomotive pressure compresses plasma at greater-than-critical density, leading to a steepening of the interface. At the same time, the backward pressure of MeV electrons near the point of absorption accelerates low-density plasma away from the interaction region and thereby reduces absorption over a time scale that is determined by the plasma gradient length and laser parameters, typically subpicosecond. Recent simulations/experiments at such intensities have demonstrated that compression of preformed plasma can lead to dominant coupling into a subMeV electron population [11] as well as laser-driven shock waves [14]. Near the interface electrons are accelerated in a combination of the standing-wave pattern of the incoming and reflected laser pulse and the electrostatic field that is generated by the presence of hot-electrons near a steep plasma interface. This mechanism, which we have identified as the most important one for the absorption of s-polarized laser pulses at dense-plasma interfaces, yields a maximum electron energy corresponding to the laser ponderomotive potential.

In underdense plasma electrons can be accelerated into quasithermal spectra extending far beyond the ponderomotive potential, due to a combination of particle acceleration in counterpropagating light waves and dephasing effects mediated by longitudinal plasma waves over tens of plasma wavelengths. When these hot-electrons pass through the electrostatic potential well in front of the solid density plasma, they are down shifted in energy to the energetically insignificant "hot tail" distributions observed inside the target.

Our one-dimensional description oversimplifies the dynamics of the critical interface and electron acceleration and always underestimates absorption due to the absence of filamentary structures [28]. The degree to which the hydrodynamic response of the preplasma to the laser pulse is one dimensional is determined by the ratio of the laser spot size to the preplasma scale length. On top of this, we expect that the main differences between our one-dimensional results and a full three-dimensional description are (1) large magnetic fields that are caused by filamenting electron beams near the point of absorption; (2) additional degrees of freedom in configuration space allow plasma expansion in the transverse direction causing the steepening effect to be less severe than in 1D; and (3) finite divergence of the laser-accelerated electrons. Long-term studies of the dynamics of the critical interface, relevant to studying the role of density profile steepening over several picoseconds, require very large volumes of plasma to be included in simulations or advanced boundary conditions for the energetic electrons reaching the boundary of the simulation box. It is important to avoid refluxing or numerical effects, which would modify the pressure balance at the critical interface in an unphysical way. These methods are currently subject of further studies.

ACKNOWLEDGMENTS

A.K. acknowledges stimulating discussions with L. Divol, M. Key, W. Kruer, H. Ruhl, and S. Wilks. This work was performed under the auspices of the U.S. Department of Energy by Lawrence Livermore National Laboratory under Contract No. DE-AC52-07NA27344. This work was funded by the Laboratory Directed Research and Development Program at LLNL under project tracking code 08-ERD-040.

[1] M. Tabak *et al.*, Phys. Plasmas **1**, 1626 (1994).
[2] W. Theobald *et al.*, Phys. Plasmas **13**, 043102 (2006).
[3] A. J. Kemp, Y. Sentoku, and M. Tabak, Phys. Rev. Lett. **101**, 075004 (2008).
[4] W. Kruer and K. Estabrook, Phys. Fluids **28**, 430 (1985).
[5] E. Lefebvre and G. Bonnaud, Phys. Rev. Lett. **74**, 2002 (1995).
[6] A. Pukhov and J. Meyer-ter-Vehn, Phys. Rev. Lett. **76**, 3975 (1996).
[7] Y. Sentoku, W. Kruer, T. Matsuoka, and A. Pukhov, Fusion Sci. Technol. **49**, 278 (2006).
[8] S. C. Wilks, W. L. Kruer, M. Tabak, and A. B. Langdon, Phys. Rev. Lett. **69**, 1383 (1992).
[9] R. Pfund, R. Lichters, and J. Meyer-ter-Vehn, in *Superstrong Fields in Plasmas*, AIP Conf. Proc. No. 426, edited by M. Lontano and D. Batani (American Institute of Physics, New York, 1998), p. 141.
[10] S. C. Wilks and W. Kruer, IEEE J. Quantum Electron. **33**, 1954 (1997).
[11] B. Chrisman, Y. Sentoku, and A. J. Kemp, Phys. Plasmas **15**, 056309 (2008).
[12] L. O. Silva, M. Marti, J. R. Davies, R. A. Fonseca, C. Ren, F. Tsung, and W. B. Mori, Phys. Rev. Lett. **92**, 015002 (2004).
[13] J. Denavit, Phys. Rev. Lett. **69**, 3052 (1992).
[14] K. U. Akli *et al.*, Phys. Rev. Lett. **100**, 165002 (2008).
[15] A. Gurevich and A. Meshcherkin, Sov. Phys. JETP **53**, 937 (1981).
[16] M. Born and E. Wolf, *Principles of Optics* (Pergamon, New York, 1975).
[17] Y. Ping, R. Shepherd, B. F. Lasinski, M. Tabak, H. Chen, H. K. Chung, K. B. Fournier, S. B. Hansen, A. Kemp, K. Widmann, S. C. Wilks, W. Rozmus, and M. Sherlock, Phys. Rev. Lett. **100**, 085004 (2008).
[18] P. Parks and T. E. Cowan, Phys. Plasmas **14**, 013102 (2007).
[19] F. Brunel, Phys. Rev. Lett. **59**, 52 (1987).
[20] P. Gibbon and A. R. Bell, Phys. Rev. Lett. **68**, 1535 (1992).
[21] M. G. Haines, M. S. Wei, F. N. Beg, and R. B. Stephens, Phys. Rev. Lett. **102**, 045008 (2009).
[22] C. Schroeder, E. Esarey, B. A. Shadwick, and W. Leemans, Phys. Plasmas **13**, 033103 (2006).
[23] J. T. Mendonca, Phys. Rev. A **28**, 3592 (1983).
[24] Z. M. Sheng, K. Mima, Y. Sentoku, M. S. Jovanović, T. Taguchi, J. Zhang, and J. Meyer-ter-Vehn, Phys. Rev. Lett. **88**, 055004 (2002).
[25] A. Bourdier, D. Patin, and E. Lefebvre, Laser Part. Beams **25**, 169 (2007).
[26] B. Bezzerides, S. Gitomer, and D. Forslund, Phys. Rev. Lett. **44**, 651 (1980).
[27] E. Sarachik and G. Schappert, Phys. Rev. D **1**, 2738 (1970).
[28] Y. Sentoku, K. Mima, S. Kojima, and H. Ruhl, Phys. Plasmas **7**, 689 (2000).